INORGANIC CHEMISTRY FRONTIERS

RESEARCH ARTICLE

View Article Online
View Journal | View Issue

Cite this: *Inorg. Chem. Front.*, 2023, **10**, 2708

Atomically isolated and unsaturated Sb sites created on Sb_2S_3 for highly selective NO electroreduction to NH_3†

Kai Chen, Ying Zhang, Wenyu Du, Yali Guo and Ke Chu *

Received 14th February 2023,
Accepted 28th March 2023

DOI: 10.1039/d3qi00268c

rsc.li/frontiers-inorganic

Sb_2S_3 comprising an atomically isolated and unsaturated Sb (Sb_{AIU}) site is demonstrated as a fascinating catalyst for highly selective electrochemical NO-to-NH_3 conversion (NORR). Theoretical calculations reveal the crucial function of Sb_{AIU} sites to favor the adsorption and activation of NO, accelerate the protonation energetics of the NO-to-NH_3 pathway and impede the coverage of H_2O/H species, thereby boosting both NORR activity and selectivity. Consequently, the developed Sb_{AIU}-rich Sb_2S_3 catalyst exhibits an excellent NO-to-NH_3 faradaic efficiency of 93.7% and a high NH_3 yield rate of 168.6 μmol h^{-1} cm^{-2}, representing the highest NORR selectivity among all reported NORR catalysts.

1. Introduction

Ammonia is a pivotal chemical that is widely applied in many aspects of social and economic development.[1–3] Recently, N_2 electrofixation emerged as a promising technology for green NH_3 synthesis, whereas its efficiency is greatly limited by intractable issues of ultrastable N≡N bonds.[4–10] Alternatively, NO possesses a relatively low N=O bond energy and thus electrochemical NO-to-NH_3 conversion (NORR) represents a more prospective approach than N_2 electrofixation for NH_3 electrosynthesis.[11–14] Nevertheless, the NORR effectiveness is greatly retarded by the sophisticated five-electron reaction process and severe competition from the hydrogen evolution reaction (HER),[1] and it is imperative to explore efficient NORR electrocatalysts capable of boosting the NO-to-NH_3 pathway with high selectivity.[15–20]

Transition metal-based catalysts commonly exhibit high NORR activity owing to their partially occupied d-orbitals boosting NO adsorption.[21–27] Nevertheless, d-orbitals also favor the formation of metal–H bonds to trigger the competitive HER, giving rise to low NORR selectivity.[28] Promisingly, main group p-block metals (Sb, In, Bi, *etc.*) are catalytically inert in the HER because of their closed d-band shells.[29] Meanwhile, the partially occupied p-orbitals in p-block metals are confirmed to be active for N=O bond dissociation, making p-block metal-based materials promising as a new class of NORR catalysts.[30–34] P-block Sb-based catalysts are appealing NORR candidates owing to the great capability of Sb sites to impede the HER and activate the nitrogen-containing molecules.[35] On the other hand, catalysts with atomically isolated sites are known to present outstanding catalytic performance because of their high atom utilization and optimal binding with intermediates and reactants.[36–38] Besides, defect engineering by creating vacancies or unsaturated sites is considered an effective strategy to tailor the electronic structure of catalysts with enhanced catalytic activities.[39–41] In view of the above, creating atomically isolated and unsaturated Sb sites is therefore an attractive strategy for designing high-efficiency NORR catalysts.

In this study, p-block Sb_2S_3 is designed as a fascinating catalyst for highly selective NORR, which exhibits an excellent NO-to-NH_3 faradaic efficiency (FE_{NH_3}) of 93.7% and a high NH_3 yield rate of 168.6 μmol h^{-1} cm^{-2}, representing the highest NORR selectivity among all reported NORR catalysts. Detailed structural characterization and theoretical computations reveal that atomically isolated and unsaturated Sb sites created on Sb_2S_3 play a crucial role in greatly enhancing the NORR activity and selectivity.

2. Results and discussion

A solvothermal method was utilized to synthesize Sb_2S_3. The XRD pattern of the as-synthesized Sb_2S_3 (Fig. 1a) shows distinct peaks that are assigned to the pure orthorhombic Sb_2S_3 phase with a good crystallinity. The SEM image of Sb_2S_3 (Fig. 1b) shows a typical nanoflower morphology consisting of numerous vertically aligned nanosheets. The nanosheet feature can be further confirmed by the TEM image (Fig. 1c).

School of Materials Science and Engineering, Lanzhou Jiaotong University, Lanzhou 730070, China. E-mail: chuk630@mail.lzjtu.cn

† Electronic supplementary information (ESI) available. See DOI: https://doi.org/10.1039/d3qi00268c

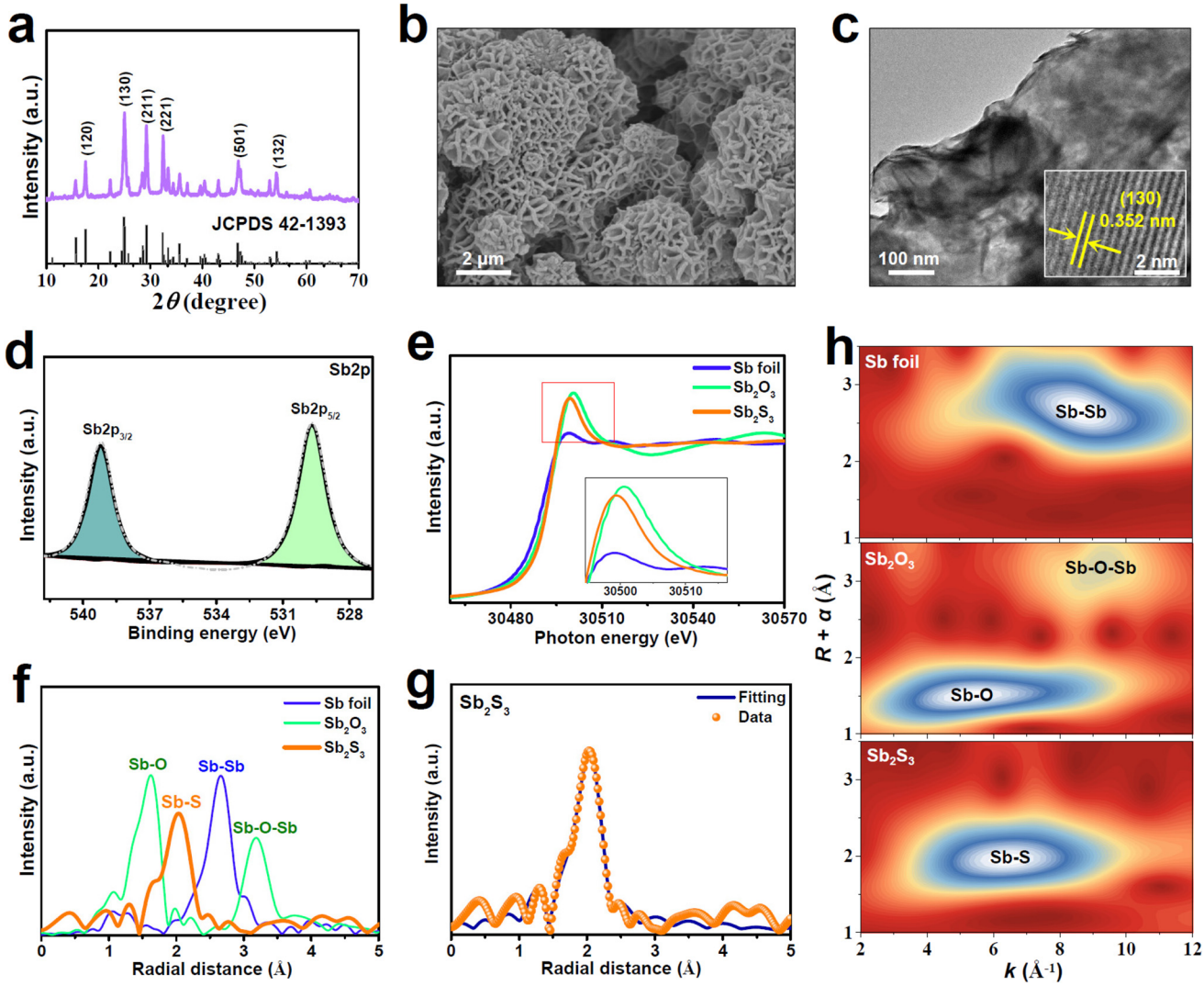

Fig. 1 Characterization of Sb_2S_3: (a) XRD pattern, (b) SEM image, (c) TEM image and HRTEM image (inset), (d) XPS Sb2p spectrum, (e) Sb K-edge XANES spectra, (f) EXAFS spectra and (h) WT profiles of Sb_2S_3 and reference samples. (g) EXAFS fitting curve of Sb_2S_3.

As shown in the HRTEM image (Fig. 1c, inset), the lattice spacing of Sb_2S_3 nanosheets is determined to be 0.352 nm, corresponding to the (130) facet of orthorhombic Sb_2S_3, in line with the XRD result (Fig. 1a). The XPS Sb spectrum of Sb_2S_3 (Fig. 1d) can be split into $Sb^{3+}2p_{3/2}$ (539.3 eV) and $Sb^{3+}2p_{5/2}$ (529.8 eV), while the deconvolution of the S2p spectrum (Fig. S1†) shows two peaks of $S2p_{1/2}$ (163.6 eV) and $S2p_{3/2}$ (161.8 eV), in good accordance with those reported for Sb_2S_3.[42–44]

We employ X-ray absorption near-edge structure (XANES) and extended X-ray absorption fine structure (EXAFS) characterizations to further examine the valence states and coordination structures of Sb_2S_3. The Sb K-edge XANES spectra (Fig. 1e) show that the white line of Sb_2S_3 is slightly lower than that of Sb_2O_3, suggesting the valence state of Sb to be smaller than the intrinsic Sb valence of Sb_2S_3 (+3), which is caused by the presence of coordinatively unsaturated Sb sites in Sb_2S_3. The Sb K-edge EXAFS spectra (Fig. 1f) show that Sb_2S_3 exhibits a dominant peak at 2.03 Å assignable to the Sb–S bond, which largely differs from those of Sb foil (Sb–Sb: 2.66 Å) and Sb_2O_3 (Sb–O: 1.62 Å, Sb–O–Sb: 3.18 Å), indicating that Sb_2S_3 comprises the isolated state of Sb and no oxidized Sb species are present on Sb_2S_3. Likewise, the corresponding wavelet transform (WT) contour plots (Fig. 1h) show only one intensity maximum at 6.3 $Å^{-1}$ corresponding to the Sb–S coordination, suggesting the existence of atomically dispersed Sb atoms. The EXAFS fitting data (Fig. 1g and Table S1†) reveal the average coordination number (CN) of Sb_2S_3 to be 4.2, much smaller than the crystallographic value of Sb_2S_3 (CN = 5),[45] corroborating the existence of plentiful unsaturated Sb sites in Sb_2S_3. These XAS results reveal that the prepared Sb_2S_3 naturally contains abundant atomically isolated and unsaturated Sb (Sb_{AIU}) sites, which are considered to be catalytically active towards NORR.

Electrocatalytic NORR measurements were carried out using a gas-tight H-type electrolytic cell containing 0.5 M Na_2SO_4 solution.[46] Several colorimetric approaches (Fig. S2 and S3†) were performed to detect the liquid products, while the gaseous products were detected by gas chromatography. We conducted linear sweep voltammetry (LSV) measurement to initially assess the NORR activity of Sb_2S_3. It is displayed in Fig. 2a that Sb_2S_3 presents a noticeable current density (j) enhancement in the NO-saturated electrolyte relative to the Ar-saturated one, proving that Sb_2S_3 has a high NORR activity. We then quantitatively determined the NORR performance of Sb_2S_3 with the integration of chronoamperometry (Fig. 2b) and colorimetric tests at various potentials. As shown in Fig. 2c, with increasing the potential, both the NH_3 yield rate and

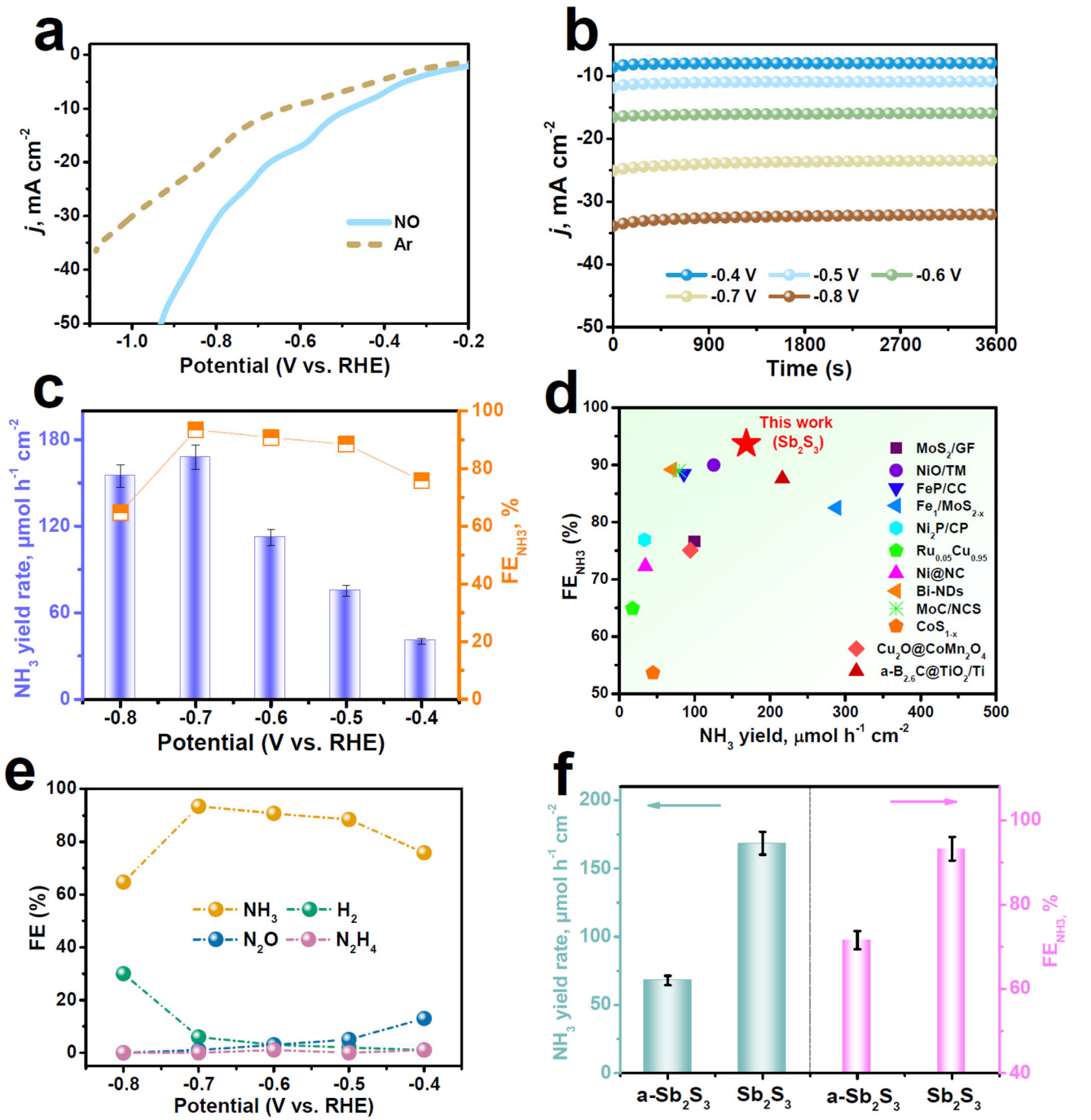

Fig. 2 (a) LSV curves of Sb_2S_3 in Ar/NO-saturated 0.5 M Na_2SO_4. (b) Chronoamperometry test of Sb_2S_3 at various potentials, and the resulting (c) NH_3 yield rates and FE_{NH_3}. (d) Comparison of NH_3 yield rates and FE_{NH_3} between Sb_2S_3 and the recently reported NORR catalysts. (e) FEs of different products on Sb_2S_3 after NORR electrolysis at various potentials. (f) NH_3 yield rates and FE_{NH_3} of Sb_2S_3 and a-Sb_2S_3 at −0.7 V.

FE_{NH_3} of Sb_2S_3 exhibit a volcanic shape and reach their highest values of 168.6 μmol h^{-1} cm^{-2} and 93.7% at −0.7 V, respectively. Strikingly, as shown in Fig. 2d (see Table S2 for details†), the FE_{NH_3} of Sb_2S_3 shows the highest NORR selectivity among all the reported NORR catalysts, while its NH_3 yield rate is also superior to those of most reported NORR catalysts. Meanwhile, Fig. 2e shows that the FEs of N-containing side products (N_2O and N_2H_4) are rather low at all considered potentials, in good accordance with the partial current density data (Fig. S4†), signifying the outstanding NO-to-NH_3 selectivity of Sb_2S_3. Regarding the NORR stability, the chronopotentiometric test presents a stable current density for at least 20 h of electrolysis

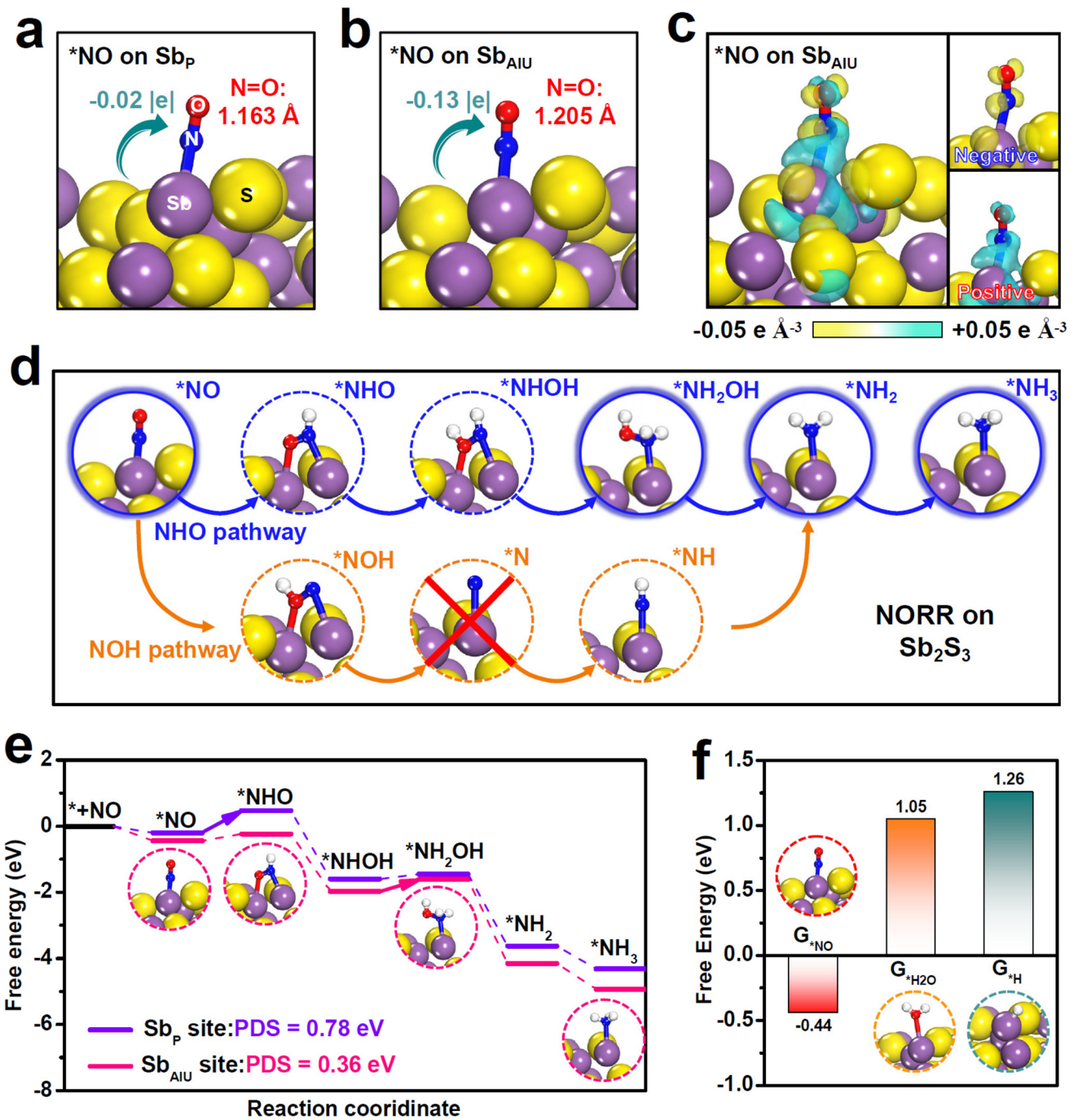

Fig. 3 (a and b) Atomic structures of absorbed NO on (a) the Sb_P site and (b) the Sb_{AlU} site of Sb_2S_3. (c) Charge density difference of *NO on the Sb_{AlU} site (yellow: accumulation; cyan: depletion). (d) Schematic of two NORR pathways (NHO and NOH) on Sb_2S_3. (e) Free energy profiles of the NORR process (NHO pathway) on Sb_P and Sb_{AlU}. (f) Binding free energies of *H_2O, *H and *NO on Sb_{AlU}.

(Fig. S5†), and the resulting FE_{NH_3} shows very small attenuations, indicating the good long-term stability of Sb_2S_3. Besides, no remarkable fluctuations in the NH_3 yield rate and FE_{NH_3} occur during the seven electrolysis cycles (Fig. S6†), proving the favorable cycling stability of Sb_2S_3.[47–50]

We conducted several experiments to verify the NH_3 origin. First, NH_3 is almost undetectable in the control colorimetric tests (Fig. S7†).[32] In addition, upon feeding ^{15}NO gas, the resulting ^1H nuclear magnetic resonance (NMR, Fig. S8†) spectra reveal the characteristic $^{15}NH_4^+$ doublets, whereas feeding Ar gas leads to the absence of $^{15}NH_4^+$ doublets.[51–53] Furthermore, the switching NO–Ar test (Fig. S9†) reveals significant NH_3 production in NO cycles, whereas NH_3 is nearly undetectable in Ar cycles. All these results validate that the produced NH_3 stems from the electrochemical NORR process catalyzed by Sb_2S_3.

For comparison, we evaluated the NORR property of annealed Sb_2S_3 (a-Sb_2S_3) with much reduced Sb_{AIU} (Fig. S10 and Table S1†) under identical measurement conditions at −0.7 V. Impressively, Fig. 2f shows that the NORR performance of a-Sb_2S_3 is significantly poorer than that of the original Sb_2S_3, revealing that the Sb_{AIU} sites play a vital role in dramatically boosting the NORR property of Sb_2S_3. Electrochemical surface area (ECSA, Fig. S11 and S12†) measurements show that the ECSA-normalized NORR performances of the two catalysts (Fig. S13†) present the same trend as that shown in Fig. 2f. Besides, both catalysts have comparable charge transport kinetics (Fig. S14†).[54–57] These findings demonstrate the intrinsic superior NORR property of Sb_2S_3.

Theoretical computations were carried out to shed light on the boosted NORR property of Sb_2S_3. To start, we evaluated the adsorption behaviors of the NO molecule on two sites of Sb_2S_3, namely the pristine Sb (Sb_P) site and the Sb_{AIU} site, as the NO adsorption is the initial critical step to trigger the NORR.[46] Upon absorbing NO on the Sb_P site (Fig. 3a), *NO exhibits a rather small N═O elongation (1.163 Å, 1.159 Å for original NO) with negligible Sb_p-to-*NO electron transfer (−0.02 |e|), which means poor NO adsorption on the Sb_P site. As a sharp comparison, *NO on the Sb_{AIU} site (Fig. 3b) presents dramatic N═O bond elongation (1.205 Å) and Sb_{AIU}-to-*NO electron transfer (−0.13 |e|), indicating largely improved NO adsorption on Sb_{AIU}. Additionally, the charge density difference (Fig. 3c) clearly shows strong *NO/Sb_{AIU} electronic interactions, where both remarkable positive and negative charge aggregations can be seen on *NO, proving that Sb_{AIU} enables powerful NO activation *via* a "donation–backdonation" mechanism.

To investigate the entire NORR process, we initially conducted online differential electrochemical mass spectrometry (DEMS) measurements to experimentally probe the reaction intermediates formed on Sb_2S_3 during the NORR electrolysis. The online DEMS spectra (Fig. S15†) reveal the generation of distinct NH_3 (m/z = 17) and NH_2OH (m/z = 33) signals.

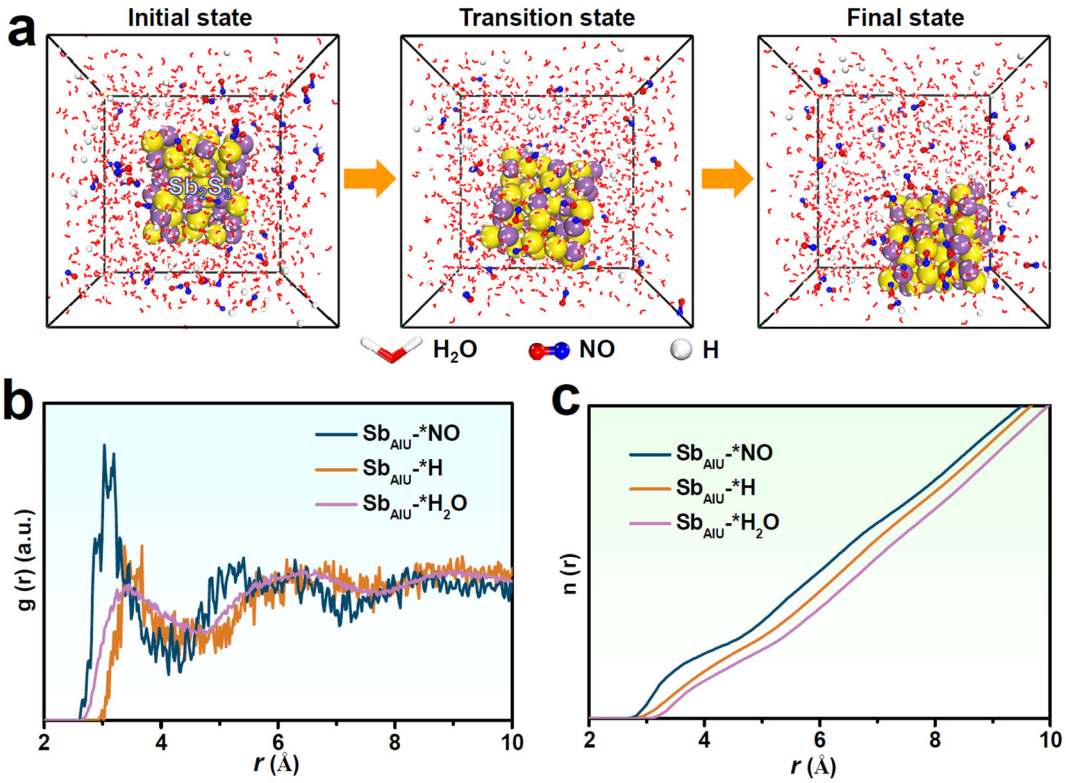

Fig. 4 (a) Initial, transition and final simulated states of the dynamic adsorption process of *H_2O, *H and *NO on Sb_{AIU}, and the corresponding (b) RDF and (c) integrated RDF curves of the interactions between Sb_{AIU} and *NO, *H and *H_2O.

Specifically, N (m/z = 14), which is the key intermediate involved in the NOH pathway, is absent in the NORR electrolysis, demonstrating that Sb_2S_3 preferentially undergoes the NHO pathway to drive the NORR process,[58] as illustrated in Fig. 3d. As displayed in the free energy profiles of the energetic-preferred NHO pathway (Fig. 3e and Fig. S16†), the Sb_p site exhibits a large energy barrier of 0.78 eV to drive the first protonation step of *NO → *NOH as the potential-determining step (PDS). In stark contrast, by virtue of powerful NO activation, the Sb_{AIU} site presents a largely reduced barrier of 0.21 eV for the same *NO → *NOH, suggesting that the initial protonation step can be greatly boosted on the Sb_{AIU} site. The PDS of Sb_{AIU} is changed to *NHOH → *NH_2OH with only 0.36 eV uphill, corroborating the significantly enhanced NORR energetics over the Sb_{AIU} site that renders a high NORR activity of Sb_2S_3. We then investigated the catalytic behavior of the Sb_{AIU} site towards the HER, which is the main competitive reaction for NORR.[24] The calculated binding free energies (G) of various species (Fig. 3f) show that G_{*NO} (−0.44 eV) is much more negative than G_{*H_2O} (1.05 eV) and G_{*H} (1.26 eV), demonstrating that the Sb_{AIU} site preferentially absorbs NO over H_2O/H species to impede the competing HER.

Molecular dynamics (MD) simulations were conducted to further examine the competitive adsorption of NO and H_2O/H on Sb_{AIU}. After simulation, the snapshots (Fig. 4a) show prominent NO aggregation on Sb_{AIU} together with an enhanced Sb_{AIU}–*NO interaction over Sb_{AIU}–*H_2O and Sb_{AIU}–*H interactions, as displayed in the radial distribution function (RDF, Fig. 4b) curves and the corresponding integrated RDF curves (Fig. 4c),[58–62] proving a high tendency of Sb_{AIU} for the adsorption and coverage of NO over H_2O/H, which is greatly favorable for HER suppression to obtain a high NORR selectivity.

3. Conclusion

In summary, Sb_{AIU}-rich Sb_2S_3 has been corroborated as a high-performing p-block metal catalyst for NORR. Theoretical computations reveal the critical role of Sb_{AIU} sites in promoting the activation and protonation of NO, while concurrently prohibiting the coverage of H_2O/H species. This work not only highlights the critical design of atomically isolated and unsaturated sites to dramatically enhance the catalytic NORR activity and selectivity, but also demonstrates the promising prospects of p-block metal elements in the design of high-efficiency NORR electrocatalysts.

Conflicts of interest

There are no conflicts of interest to declare.

Acknowledgements

This work was supported by the Longyuan Youth Innovative and Entrepreneurial Talents Project ([2021]17).

References

1 J. Liang, Q. Liu, A. A. Alshehri and X. Sun, Recent advances in nanostructured heterogeneous catalysts for N-cycle electrocatalysis, *Nano Res. Energy*, 2022, **1**, e9120010.
2 G. Wang, P. Shen, Y. Luo, X. Li, X. Li and K. Chu, A vacancy engineered MnO_{2-x} electrocatalyst promotes electroreduction of nitrate to ammonia, *Dalton Trans.*, 2022, **51**, 9206–9212.
3 X. Zhao, G. Hu, G. F. Chen, H. Zhang, S. Zhang and H. Wang, Comprehensive understanding of the thriving ambient electrochemical nitrogen reduction reaction, *Adv. Mater.*, 2021, **33**, 2007650.
4 Y. Luo, P. Shen, X. Li, Y. Guo and K. Chu, Sulfur-deficient Bi_2S_{3-x} synergistically coupling $Ti_3C_2T_x$-MXene for boosting electrocatalytic N_2 reduction, *Nano Res.*, 2022, **15**, 3991–3999.
5 Y. Luo, Q. Li, Y. Tian, Y. Liu and K. Chu, Amorphization engineered VSe_{2-x} nanosheets with abundant Se-vacancies for enhanced N_2 electroreduction, *J. Mater. Chem. A*, 2022, **10**, 1742–1749.
6 K. Chu, Y. Luo, P. Shen, X. Li, Q. Li and Y. Guo, Unveiling the synergy of O-vacancy and heterostructure over MoO_{3-x}/MXene for N_2 electroreduction to NH_3, *Adv. Energy Mater.*, 2022, **12**, 2103022.
7 Y. Cheng, X. Li, P. Shen, Y. Guo and K. Chu, MXene quantum dots/copper heterostructure for synergistically enhanced N_2 electroreduction, *Energy Environ. Mater.*, 2023, **6**, e12268.
8 Z. Yan, M. Ji, J. Xia and H. Zhu, Recent advanced materials for electrochemical and photoelectrochemical synthesis of ammonia from dinitrogen: One step closer to a sustainable energy future, *Adv. Energy Mater.*, 2020, **10**, 1902020.
9 K. Tanifuji and Y. Ohki, Metal–sulfur compounds in N_2 reduction and nitrogenase-related chemistry, *Chem. Rev.*, 2020, **120**, 5194–5251.
10 G. Qing, R. Ghazfar, S. T. Jackowski, F. Habibzadeh, M. M. Ashtiani, C.-P. Chen, M. R. Smith and T. W. Hamann, Recent advances and challenges of electrocatalytic N_2 reduction to ammonia, *Chem. Rev.*, 2020, **120**, 5437–5516.
11 B. H. Ko, B. Hasa, H. Shin, Y. Zhao and F. Jiao, Electrochemical reduction of gaseous nitrogen oxides on transition metals at ambient conditions, *J. Am. Chem. Soc.*, 2022, **144**, 1258–1266.
12 J. Long, S. Chen, Y. Zhang, C. Guo, X. Fu, D. Deng and J. Xiao, Direct electrochemical ammonia synthesis from nitric oxide, *Angew. Chem., Int. Ed.*, 2020, **59**, 9711–9718.
13 J. Choi, H.-L. Du, C. K. Nguyen, B. H. R. Suryanto, A. N. Simonov and D. R. MacFarlane, Electroreduction of nitrates, nitrites, and gaseous nitrogen oxides: A potential source of ammonia in dinitrogen reduction studies, *ACS Energy Lett.*, 2020, **5**, 2095–2097.
14 Y. Xiong, Y. Li, S. Wan, Y. Yu, S. Zhang and Q. Zhong, Ferrous-based electrolyte for simultaneous NO absorption

and electroreduction to NH_3 using Au/rGO electrode, *J. Hazard. Mater.*, 2022, **430**, 128451.
15 W. Zhang, X. Qin, T. Wei, Q. Liu, J. Luo and X. Liu, Single atomic cerium sites anchored on nitrogen-doped hollow carbon spheres for highly selective electroreduction of nitric oxide to ammonia, *J. Colloid Interface Sci.*, 2023, **638**, 650–657.
16 J. Liang, P. Liu, Q. Li, T. Li, L. Yue, Y. Luo, Q. Liu, N. Li, B. Tang, A. A. Alshehri, I. Shakir, P. O. Agboola, C. Sun and X. Sun, Amorphous boron carbide on titanium dioxide nanobelt arrays for high-efficiency electrocatalytic NO reduction to NH_3, *Angew. Chem., Int. Ed.*, 2022, **61**, e202202087.
17 Q. Wu, H. Wang, S. Shen, B. Huang, Y. Dai and Y. Ma, Efficient nitric oxide reduction to ammonia on a metal-free electrocatalyst, *J. Mater. Chem. A*, 2021, **9**, 5434–5441.
18 J. Long, C. Guo, X. Fu, H. Jing, G. Qin, H. Li and J. Xiao, Unveiling potential dependence in NO electroreduction to ammonia, *J. Phys. Chem. Lett.*, 2021, **12**, 6988–6995.
19 S. Cheon, W. J. Kim, D. Y. Kim, Y. Kwon and J.-I. Han, Electro-synthesis of ammonia from dilute nitric oxide on a gas diffusion electrode, *ACS Energy Lett.*, 2022, **7**, 958–965.
20 Y. Xiao and C. Shen, Transition-metal borides (MBenes) as new high-efficiency catalysts for nitric oxide electroreduction to ammonia by a high-throughput approach, *Small*, 2021, **17**, 2100776.
21 T. Wei, H. Bao, X. Wang, S. Zhang, Q. Liu, J. Luo and X. Liu, Ionic liquid-assisted electrocatalytic NO reduction to NH_3 by P-doped MoS_2, *ChemCatChem*, 2023, **15**, e202201411.
22 D. Qi, F. Lv, T. Wei, M. Jin, G. Meng, S. Zhang, Q. Liu, W. Liu, D. Ma, M. S. Hamdy, J. Luo and X. Liu, High-efficiency electrocatalytic NO reduction to NH_3 by nanoporous VN, *Nano Res. Energy*, 2022, **1**, e9120022.
23 J. Liang, Q. Zhou, T. Mou, H. Chen, L. Yue, Y. Luo, Q. Liu, M. S. Hamdy, A. A. Alshehri, F. Gong and X. Sun, FeP nanorod array: A high-efficiency catalyst for electroreduction of NO to NH_3 under ambient conditions, *Nano Res.*, 2022, **15**, 4008–4013.
24 K. Chen, G. Zhang, X. Li, X. Zhao and K. Chu, Electrochemical NO reduction to NH_3 on Cu single atom catalyst, *Nano Res.*, 2023, DOI: **10.1007/s12274-023-5384-9**.
25 K. Chen, J. Wang, H. Zhang, D. Ma and K. Chu, Self-tandem electrocatalytic NO reduction to NH_3 on a W single-atom catalyst, *Nano Lett.*, 2023, **23**, 1735–1742.
26 K. Chen, Y. Tian, Y. Li, Y.-P. Liu and K. Chu, Amorphous NiB_2 for electroreduction of NO to NH_3, *J. Mater. Chem. A*, 2023, **11**, 7409–7414.
27 K. Chen, P. Shen, N. Zhang, D. Ma and K. Chu, Electrocatalytic NO reduction to NH_3 on Mo_2C nanosheets, *Inorg. Chem.*, 2023, **62**, 653–658.
28 Y. Sun, Y. Wang, H. Li, W. Zhang, X.-M. Song, D.-M. Feng, X. Sun, B. Jia, H. Mao and T. Ma, Main group metal elements for ambient-condition electrochemical nitrogen reduction, *J. Energy Chem.*, 2021, **62**, 51–70.
29 L. Li, C. Tang, H. Jin, K. Davey and S.-Z. Qiao, Main-group elements boost electrochemical nitrogen fixation, *Chem*, 2021, **7**, 3232–3255.
30 C. Lv, J. Liu, C. Lee, Q. Zhu, J. Xu, H. Pan, C. Xue and Q. Yan, Emerging p-block-element-based electrocatalysts for sustainable nitrogen conversion, *ACS Nano*, 2022, **16**, 15512–15527.
31 X. Li, G. Zhang, P. Shen, X. Zhao and K. Chu, A defect engineered p-block SnS_{2-x} catalyst for efficient electrocatalytic NO reduction to NH_3, *Inorg. Chem. Front.*, 2023, **10**, 280–287.
32 K. Chen, Y. Zhang, J. Xiang, X. Zhao, X. Li and K. Chu, p-block antimony single-atom catalysts for nitric oxide electroreduction to ammonia, *ACS Energy Lett.*, 2023, **8**, 1281–1288.
33 K. Chen, G. Wang, Y. Guo, D. Ma and K. Chu, Iridium single-atom catalyst for highly efficient NO electroreduction to NH_3, *Nano Res.*, 2023, DOI: **10.1007/s12274-023-5556-7**.
34 K. Chen, N. Zhang, F. Wang, J. Kang and K. Chu, Main-group indium single-atom catalysts for efficient electrocatalytic NO reduction to NH_3, *J. Mater. Chem. A*, 2023, **11**, 6814–6819.
35 X. Liu, H. Jang, P. Li, J. Wang, Q. Qin, M. G. Kim, G. Li and J. Cho, Antimony-based composites loaded on phosphorus-doped carbon for boosting Faradaic efficiency of the electrochemical nitrogen reduction reaction, *Angew. Chem., Int. Ed.*, 2019, **58**, 13329–13334.
36 S. K. Kaiser, Z. Chen, D. Faust Akl, S. Mitchell and J. Pérez-Ramírez, Single-atom catalysts across the periodic table, *Chem. Rev.*, 2020, **120**, 11703–11809.
37 C. Gao, J. Low, R. Long, T. Kong, J. Zhu and Y. Xiong, Heterogeneous single-atom photocatalysts: fundamentals and applications, *Chem. Rev.*, 2020, **120**, 12175–12216.
38 L. Zhang, M. Zhou, A. Wang and T. Zhang, Selective hydrogenation over supported metal catalysts: from nanoparticles to single atoms, *Chem. Rev.*, 2019, **120**, 683–733.
39 Q. Li, Y. Guo, Y. Tian, W. Liu and K. Chu, Activating VS_2 basal planes for enhanced NRR electrocatalysis: the synergistic role of S-vacancies and B dopants, *J. Mater. Chem. A*, 2020, **8**, 16195–16202.
40 K. Chu, J. Wang, Y. Liu, Q. Li and Y. Guo, Mo-doped SnS_2 with rich S-vacancies for highly efficient electrocatalytic N_2 reduction: the critical role of Mo-Sn-Sn trimer, *J. Mater. Chem. A*, 2020, **8**, 7117–7124.
41 H. Du, H. Guo, K. Wang, X. Du, B. A. Beshiwork, S. Sun, Y. Luo, Q. Liu, T. Li and X. Sun, Durable electrocatalytic reduction of nitrate to ammonia over defective pseudobrookite Fe_2TiO_5 nanofibers with abundant oxygen vacancies, *Angew. Chem., Int. Ed.*, 2023, **135**, e202215782.
42 A. Maiti and S. K. Srivastava, N, Ru codoped pellet drum bundle-like Sb_2S_3: An efficient hydrogen evolution reaction and hydrogen oxidation reaction electrocatalyst in alkaline medium, *ACS Appl. Mater. Interfaces*, 2020, **12**, 7057–7070.
43 X. Chen, X. Li, P. Wei, X. Ma, Q. Yu and L. Liu, Selective synthesis of Sb_2S_3 nanostructures with different mor-

phologies for high performance in dye-sensitized solar cells, *Chin. J. Catal.*, 2020, **41**, 435–441.

44 S. Yao, J. Cui, Y. Deng, W. G. Chong, J. Wu, M. Ihsan-Ul-Haq, Y.-W. Mai and J.-K. Kim, Ultrathin Sb_2S_3 nanosheet anodes for exceptional pseudocapacitive contribution to multi-battery charge storage, *Energy Storage Mater.*, 2019, **20**, 36–45.

45 Y. S. Park, X. Jin, J. Tan, H. Lee, J. Yun, S. Ma, G. Jang, T. Kim, S. G. Shim and K. Kim, High-performance Sb_2S_3 photoanode enabling iodide oxidation reaction for unbiased photoelectrochemical solar fuel production, *Energy Environ. Sci.*, 2022, **15**, 4725–4737.

46 K. Chen, J. Wang, J. Kang, X. Lu, X. Zhao and K. Chu, Atomically Fe-doped MoS_{2-x} with Fe-Mo dual sites for efficient electrocatalytic NO reduction to NH_3, *Appl. Catal., B*, 2023, **324**, 122241.

47 L. Zhang, J. Zhang, A. Xu, Z. Lin, Z. Wang, W. Zhong, S. Shen and G. Wu, Charge redistribution of Co_9S_8/MoS_2 heterojunction microsphere enhances electrocatalytic hydrogen evolution, *Biomimetics*, 2023, **8**, 104.

48 L. Zhang, Z. Wang, J. Zhang, Z. Lin, Q. Zhang, W. Zhong and G. Wu, High activity and stability in Ni_2P/(Co,Ni)OOH heterointerface with a multiple-hierarchy structure for alkaline hydrogen evolution reaction, *Nano Res.*, 2023, DOI: 10.1007/s12274-022-5322-2.

49 X. Wang, J. Zhang, Z. Wang, Z. Lin, S. Shen and W. Zhong, Fabricating Ru single atoms and clusters on CoP for boosted hydrogen evolution reaction, *Chin. J. Struct. Chem.*, 2023, DOI: 10.1016/j.cjsc.2023.100035.

50 Y. Huang, Z. Hu, L.-a. Huang, Z. Wang, Z. Lin, S. Shen, W. Zhong and J. Pan, Phosphorus-modified cobalt single-atom catalysts loaded on crosslinked carbon nanosheets for efficient alkaline hydrogen evolution reaction, *Nanoscale*, 2023, **15**, 3550–3559.

51 N. Zhang, G. Zhang, P. Shen, H. Zhang, D. Ma and K. Chu, Lewis acid Fe–V pairs promote nitrate electroreduction to ammonia, *Adv. Funct. Mater.*, 2023, **33**, 2211537.

52 G. Wang, P. Shen, K. Chen, Y.-L. Guo, X. Zhao and K. Chu, Rare-earth La-doped VS_{2-x} for electrochemical nitrate reduction to ammonia, *Inorg. Chem. Front.*, 2023, **10**, 2014–2021.

53 K. Chen, Z. Ma, X. Li, J. Kang, D. Ma and K. Chu, Single-atom Bi alloyed Pd metallene for nitrate electroreduction to ammonia, *Adv. Funct. Mater.*, 2023, **33**, 2209890.

54 W. Zhang, M. Jiang, S. Yang, Y. Hu, B. Mu, Z. Tie and Z. Jin, *In situ* grown CuO_x nanowire forest on copper foam: A 3D hierarchical and freestanding electrocatalyst with enhanced carbonaceous product selectivity in CO_2 reduction, *Nano Res. Energy*, 2022, **1**, e9120033.

55 N. Zhang, G. Zhang, Y. Tian, Y. Guo and K. Chu, Boron phosphide as an efficient metal-free catalyst for nitrate electroreduction to ammonia, *Nano Res. Energy*, 2023, **52**, 4290–4295.

56 F. Guo, M. Zhang, S. Yi, X. Li, R. Xin, M. Yang, B. Liu, H. Chen, H. Li and Y. Liu, Metal-coordinated porous polydopamine nanospheres derived Fe_3N–FeCo encapsulated N-doped carbon as a highly efficient electrocatalyst for oxygen reduction reaction, *Nano Res. Energy*, 2022, **1**, e9120027.

57 Y. Cheng, P. Shen, X. Li, X. Li, K. Chu and Y. Guo, Synergistically enhanced peroxidase-like activity of Fe_3O_4/Ti_3C_2 MXene quantum dots and its application in colorimetric determination of Cr(VI), *Sens. Actuators, B*, 2023, **376**, 132979.

58 X. Li, K. Chen, X. Lu, D. Ma and K. Chu, Atomically dispersed Co catalyst for electrocatalytic NO reduction to NH_3, *Chem. Eng. J.*, 2023, **454**, 140333.

59 P. Shen, X. Li, Y. Luo, Y. Guo, X. Zhao and K. Chu, High-efficiency N_2 electroreduction enabled by Se-vacancy-rich WSe_{2-x} in water-in-salt electrolytes, *ACS Nano*, 2022, **16**, 7915–7925.

60 G. Zhang, X. Li, K. Chen, Y. Guo, D. Ma and K. Chu, Tandem electrocatalytic nitrate reduction to ammonia on MBenes, *Angew. Chem., Int. Ed.*, 2023, **62**, e202300054.

61 Y. Luo, K. Chen, G. Wang, G. Zhang, N. Zhang and K. Chu, Ce-doped MoS_{2-x} nanoflower arrays for electrocatalytic nitrate reduction to ammonia, *Inorg. Chem. Front.*, 2023, **10**, 1543–1551.

62 X. Li, P. Shen, X. Li, D. Ma and K. Chu, Sub-nm RuO_x clusters on Pd metallene for synergistically enhanced nitrate electroreduction to ammonia, *ACS Nano*, 2023, **17**, 1081–1090.